RNA BIOLOGY
2025, VOL. 22, NO. 1, 1–16
https://doi.org/10.1080/15476286.2025.2508107

Taylor & Francis
Taylor & Francis Group

RESEARCH PAPER

OPEN ACCESS Check for updates

RNA-seq analyses reveal the relevance of RNAs involved in ribosomal complex to induce mammalian prion protein aggregation and phase separation *in vitro*

Ana C. Tahira[a*], Mariana P. B. Gomes[b,c*], Maria Heloisa Freire[b], Marcelly Muxfeldt[b], Francisco Prosdocimi[d], Yulli M. Passos[b], Murilo Sena Amaral[a], Leticia P. Felix Valadão[b], Luciana P. Rangel[b], Jerson L. Silva[d,e], Sergio Verjovski-Almeida[a,f], and Yraima Cordeiro [b]

[a]Laboratório de Ciclo Celular, Instituto Butantan, São Paulo, Brasil; [b]Faculdade de Farmácia, Universidade Federal do Rio de Janeiro, Rio de Janeiro, Brasil; [c]Fundação Oswaldo Cruz, Instituto de Tecnologia em Imunobiológicos, Rio de Janeiro, Brasil; [d]Instituto de Bioquímica Médica Leopoldo de Meis, Universidade Federal do Rio de Janeiro, Rio de Janeiro, Brasil; [e]D'Or Institute for Research and Education (IDOR), Rio de Janeiro, RJ, Brazil; [f]Departamento de Bioquímica, Instituto de Química, Universidade de São Paulo, São Paulo, Brasil

ABSTRACT

Conformational conversion of cellular prion protein (PrP^C) into infectious PrP (PrP^{Sc}) is one of the most intriguing processes in modern Biology. It is well accepted that this transition is catalysed by one or more cofactors that lower the energy barrier between the different PrP forms. Among potential candidates, RNA molecules are strong contenders. Our group has pursued nucleic acids, both DNA and RNA, capable of inducing PrP misfolding, aggregation, and, more recently, phase separation, a process proposed to precede aggregation in degenerative disorders. We found that the interaction between recombinant PrP (rPrP) and total RNA extracted from neuroblastoma cells (N2aRNA) results in significant structural alterations. Here, we use rPrP:N2aRNA as a model to search for RNAs capable of inducing full-length murine rPrP phase separation and/or aggregation. N2aRNA was incubated with rPrP and after that, RNA-seq analysis was conducted with RNAs isolated from the insoluble material using two different protocols. We analysed thousands of RNA-seq reads, most of which represented ribosomal RNA molecules. The set of recovered molecules is heterogeneous; nevertheless, three low-complexity consensus motifs within the sequences of RNAs involved in ribosomal complex were identified as significantly enriched in the RNAs bound to rPrP, suggesting that a population of RNAs is responsible for inducing PrP phase transitions. We hypothesize that RNA transcripts enriched in a set of low complexity motif sequences with predicted structural similarities can be involved in PrP^C binding. This interaction would lead to phase separation and, ultimately, result in aggregation into scrapie-like species, in a stoichiometry-dependent manner.

ARTICLE HISTORY
Revised 1 April 2025
Accepted 1 May 2025

KEYWORDS
Prion protein; RNA-seq; ChIP-seq; prion diseases; RNA; nucleic acid; protein aggregation; liquid-liquid phase separation; neurodegenerative diseases; protein-nucleic acid interaction

Introduction

Prion diseases or Transmissible Spongiform Encephalopathies (TSEs) are a group of rare fatal neurodegenerative disorders that affect humans and other mammals [1]. The characteristic that distinguishes TSEs from other conformational diseases, such as Alzheimer's Disease (AD) and Parkinson's Disease (PD) is their proven transmissibility. However, it has been shown that misfolded proteins involved in other neurodegenerative diseases, including AD and PD, can also harbour prion-like characteristics, i.e. they can be transmitted from cell to cell and induce native proteins to acquire the abnormal conformation [2,3]. Progression of TSEs is associated with misfolding of cellular prion protein (PrP^C), a constitutive protein present in many tissues but primarily expressed in neurons and in the lymphoid system [1].

The major structural event in prion disorders is the conversion of PrP^C into its infectious form, PrP scrapie (PrP^{Sc}) [1,4]. In all sporadic manifestations of the disease, both PrP forms share the same primary structure, but exhibit significantly different physicochemical properties. While PrP^C is mostly α-helical, soluble, and fully sensitive to protease digestion, PrP^{Sc} loses most of the PrP^C α-helical content and has a higher β-sheet content, tends to form aggregates (both amyloid and non-amyloid species), and is partially resistant to protease digestion [5,6].

For decades it was believed that PrP^{Sc} was the only molecular entity needed to trigger PrP^C misfolding and aggregation, amplifying PrP^{Sc} formation [1,7]. Later, it became accepted that other molecules may play a role in the early stages of prion diseases, by assisting the conversion of PrP^C to

CONTACT Sergio Verjovski-Almeida verjo@iq.usp.br Laboratório de Ciclo Celular, Instituto Butantan, Av. Vital Brasil 1500, São Paulo 05503-900, Brazil;Yraima Cordeiro yraima@farmacia.ufrj.br Faculdade de Farmácia, UniversidadeFederal do Rio de Janeiro, Av.Carlos Chagas Filho 373, CCS, bloco B, subsolo, sala 17 São Paulo 21941-902, Brazil
*Both authors contributed equally to this work.
Supplemental data for this article can be accessed online at https://doi.org/10.1080/15476286.2025.2508107

PrP^{Sc} [8–11]. PrP^{Sc} can act as a template and refold PrP^{C} into more PrP^{Sc}, but a high-energy barrier prevents spontaneous conversion between the two forms [12]. It has been proposed that, to overcome this barrier, an additional molecule must be involved in the process, acting as a catalyst [13]. Accordingly, most *in vitro* conversion assays used to induce amplification of scrapie-like prion species include a polyanionic molecule, such as RNA, glycosaminoglycan, or an anionic lipid [9,11,13]. Based on these assays and biophysical studies, numerous molecules capable of participating in the conversion process have been identified. Among them, nucleic acids emerge as likely candidates [8,10,13–15].

It has been reported that RNA molecules are needed to propagate PrP^{Sc} *in vitro* and that RNA molecules can be found associated with infectious prion particles purified from diseased brains [10,16–19]. The observation that the ribosome can be a target for anti-prion compounds that do not bind directly to PrP [20] also strengthens the proposal of RNA modulation of PrP conversion. Although PrP is not a classical RNA-binding protein (RBP), bioinformatic analyses confirm that it has several attributes that qualify it as an RBP [21]. In addition to its binding with nucleic acids (NA), the intrinsically disordered nature of PrP positions this protein as a versatile scaffolding molecule capable of undergoing both homotypic and heterotypic (e.g.: with nucleic acids) phase separation.

It has been proposed that aberrant phase transitions may be the underlying cause of the pathogenesis of neurodegenerative diseases [22–24], where the formation of aggregated species is preceded by liquid-liquid phase separation (LLPS) [24–26]. LLPS is a phenomenon driven by weak multivalent interactions between proteins and other biomolecules, leading to the formation of dynamic, concentrated, membraneless condensates [21,23,25]. These structures arise through electrostatic interactions, π-π stacking, cation-π interactions, hydrogen bonding, and hydrophobic forces, facilitating cellular compartmentalization and the regulation of biochemical processes [21,25]. LLPS plays essential physiological roles, including the organization of membraneless organelles such as the nucleolus and stress granules, the regulation of gene transcription, cell signalling at the plasma membrane, and the modulation of cytoskeletal dynamics [23]. While LLPS is crucial for maintaining cellular homoeostasis, its dysregulation has been linked to pathological transitions associated with neurodegenerative diseases [21–24].

In the context of heterotypic PrP phase transitions, we have described that interaction with DNA aptamers drives the formation of rPrP-NA condensates [27]. Depending on the aptamer conformation, a liquid-to-solid transition was observed [27,28], possibly related to the formation of pathological protein aggregates.

In summary, rPrP can bind both DNA and RNA with (sub)micromolar affinities *in vitro* [8,14,27,29] and the resultant complexes may be phase-separated condensates [27], or aggregated species (undergoing a liquid-to-solid transition) that may induce cell dysfunction. These effects seem to depend more on NA size and conformation than on its sequence [8,27,30]. In particular, total RNA extracted from murine neuroblastoma (N2a) cells produced aggregated rPrP: RNA species with high toxicity to mammalian cultured cells [14].

Based on these findings, we asked which RNA molecules present in the total RNA extract were involved in the interaction with full-length murine recombinant PrP ($rPrP^{23–231}$, from now on referred to only as rPrP) and responsible for the previously observed effects [14]. We used total RNA extracted from N2a cells (N2aRNA) to identify sequences bound to rPrP with high affinity. N2aRNA was incubated with full-length rPrP, and insoluble samples were centrifuged. RNA was recovered from the pellet using different approaches (washing with NaCl at 250 or 350 mM and after treatment with RNase) (Figure 1). The recovered RNAs induced de novo aggregation/phase separation of rPrP and were amplified and sequenced using the Illumina platform. Across different replicates, significantly enriched rRNA motifs were found, suggesting that these molecules participate in PrP misfolding and drive PrP phase separation, which may precede pathological PrP aggregation.

Materials and methods

Reagents and protein samples

All reagents used were of analytical grade. Protein concentration was 1.0 μM (0.023 mg/mL), for light scattering (LS) measurements, 10 μM (0.23 mg/mL) for turbidity assays, and 50 μM (1.15 mg/mL) for RNA extraction assays. We used 10 mM Tris (tris(hydroxymethyl)aminomethane) buffer containing 100 mM NaCl, pH 7.4 in all experiments performed in this study. If another buffer or different protein concentration was used, it was indicated in the figure legend. Recombinant human α-synuclein was expressed and purified as described [31]. The single-stranded 25-mer DNA aptamer A1_mut [27] was synthesized and purified by Integrated DNA Technologies (Coralville, USA). All materials used were nuclease-free or previously treated with diethyl pyrocarbonate (DEPC). All figures presented in this work are representative of at least three independent experiments.

Expression and purification of recombinant prion protein, rPrP

Full-length recombinant murine PrP ($rPrP^{23–231}$) was expressed in *Escherichia coli* and further purified by high-affinity column refolding and histidine tag removal using human thrombin following previously described protocols [8,32].

Cell cultivation

Neuro2a (N2a) cell lines were purchased from the Rio de Janeiro Cell Bank (BCRJ, RJ, Brazil). Cells were grown in DMEM/F-12 medium with 10% foetal bovine serum, 0.1% gentamicin (10 mg/mL) and were maintained at 37 °C in a humidified atmosphere containing 5% CO_2.

Ribonucleic acid samples

Total RNA was extracted from N2a cells (N2aRNA) with TRIzol (Invitrogen, USA) following the manufacturer's

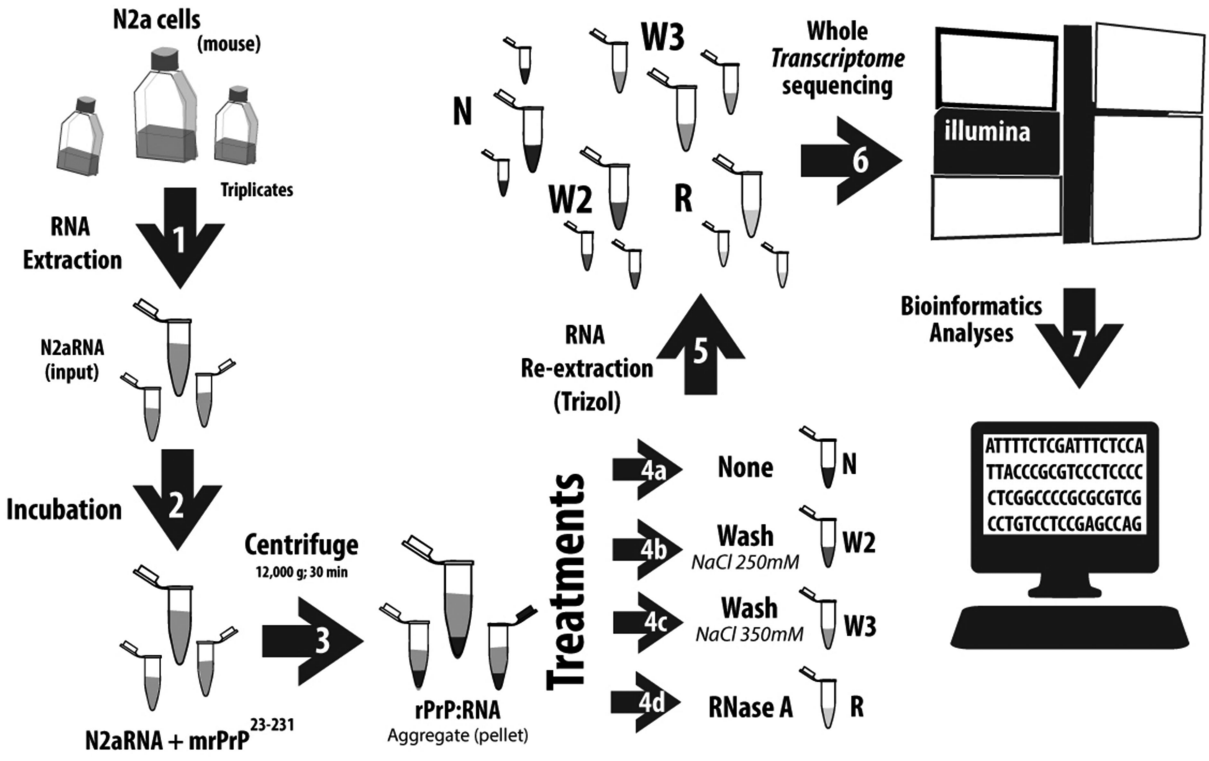

Figure 1. Strategy for RNA recovery from rPrP:N2aRNA aggregates and sequencing. Schematic representation of protocols used for RNA recovery and sequencing. After extraction from N2a cells (1), total RNA transcripts were incubated with rPrP (2), the resultant aggregate was precipitated (3) and subjected to different treatments: not treated (4a), washed with NaCl 250 mM (4b), washed with NaCl 350 mM (4c) or treated with RNase A (4d). Then, RNA molecules were re-extracted (5), and further sequenced (6), and analysed (7).

instructions. N2a cells were centrifuged at 3,200 *g* for 10 min and all supernatant was discarded. The obtained pellet was resuspended in 1 mL of TRIzol and incubated for 10 min. Subsequently, 0.2 mL of chloroform was added, homogenized, incubated for an additional 3 min, and then centrifuged for 15 min, at 10,000 *g*. At this step, the aqueous phase was transferred to a new sterile microtube (RNase free, Axygen), followed by the addition of 0.5 mL isopropanol, homogenized, incubated for 10 min, and centrifuged for 10 min, at 10,000 *g*. The pellet was washed with 1 mL 75% ethanol, vortexed vigorously to homogenize, centrifuged for 5 min, at 7,500 *g*. Subsequently, the entire supernatant was removed, and the pellet was dried at 37 °C to evaporate the ethanol. Finally, the extracted RNA was resuspended in ultrapure water treated with DEPC, incubated for 10 min at 65 °C and then quantified and stored at −20 °C. To verify the integrity of the extracted RNA, quality control was performed running the samples on a 0.8% agarose gel at 100 V, 1 h in 4-morpholinepropanesulfonic acid (MOPS) buffer and formaldehyde and stained with GelRed (Biotium, USA).

Turbidity assay

The turbidity of rPrP sample in the presence of re-extracted RNA was measured at 400 nm in a SpectraMax® Paradigm® (Molecular Devices) 96-well plate reader. The final concentration of rPrP was 10 µM (0.23 mg/mL) and the recovered RNA concentration was 0.115 mg/mL. To further investigate aggregation kinetics, additional turbidity assays were conducted in quadruplicate using a CLARIOstar (BMG LABTECH) plate reader at 400 nm, in a 384-well plate. rPrP was tested at a fixed concentration of 0.115 mg/mL (5 µM) with N2aRNA (Figure 1, input), RNase-treated N2aRNA (Figure 1 (R)), or A1_mut aptamer at 2:1 (0.0575 mg/mL) and 1:5 (0.575 mg/mL) ratios. Similarly, α-synuclein at 0.070 mg/mL (5 µM) was incubated with N2aRNA at 0.035 mg/mL (2:1) or 0.350 mg/mL (1:5). All samples were prepared in 10 mM Tris buffer at pH 7.4, containing 100 mM NaCl.

Transmission electron microscopy and optical microscopy

Micrographs of rPrP in the presence of N2aRNA (input), RNase-treated N2aRNA, or A1_mut were acquired using a FEI Tecnai SPIRIT transmission electron microscope. Sample grids were prepared by applying 5 µL of each sample onto formvar/carbon-coated grids, followed by negative staining with 2.0% uranyl acetate. To assess the presence of liquid-liquid phase separation (LLPS), bright-field microscopy was performed using a Nikon Inverted Microscope Eclipse Ti-S equipped with a 60× water-immersion objective (numerical aperture 1.2). rPrP was tested at a fixed concentration of 230 µg/mL (10 µM), and α-synuclein at 140 µg/mL (10 µM) with N2aRNA, RNase-treated N2aRNA, or A1_mut at 2:1 and 1:5 stoichiometries. A total of 20 µL of each sample was pipetted onto a 24 × 60 mm coverslip. All images were acquired at room temperature and processed using Fiji (ImageJ, USA). All samples were prepared in 10 mM Tris buffer at pH 7.4, containing 100 mM NaCl.

Droplet quantification

The quantification of images obtained through phase-contrast microscopy was performed using Fiji software (ImageJ, USA). The images were converted to 8-bit, and the contrast was adjusted to enhance droplet visualization. An edge detection filter (*Find Edges*) was applied to highlight the edges of suspended droplets. The threshold was adjusted to distinguish suspended droplets from background droplets (wetting). The suspended droplets were quantified in terms of area (μm^2) and number.

Isolation of RNA molecules bound to rPrP

rPrP (200 µg) was incubated with total RNA extracted from N2a cells (N2aRNA, input) (100 µg) for 10 min in 10 mM Tris buffer at pH 7.4, containing 100 mM NaCl. After incubation, samples were centrifuged for 30 min at 12,000 *g* to precipitate the aggregates. The pellet samples were saved and labelled as 'no treatment' samples. In parallel, aggregate pellets were washed with 250 mM or 350 mM NaCl and pelleted again (twice) or treated with 1 µg (70 units) of RNase A (Product number R6513, Sigma, USA) in 500 µL of 10 mM Tris buffer containing 100 mM NaCl at pH 7.4 for 1 h at 37 °C and pelleted again (Figure 1). RNA was recovered from each pellet using TRIzol (following the manufacturer's instructions) and quantified using a Nanodrop ND-1000 spectrophotometer (NanoDrop Technologies, Inc., USA) (Table S1).

Cytotoxicity assay

Cells were seeded in 96-well plates at 40–50% confluency. On the following day, cells were treated with the tested samples which had been prepared 21 hours earlier. The final treatment volume consisted of 10% of the sample in each well. The samples were: rPrP:N2aRNA (1:5 ratio), rPrP, and N2aRNA, with an rPrP concentration of 0.0115 mg/mL. After a 72-h treatment, MTT at 0.5 mg/mL in PBS was added, and the plates were incubated for 2–4 h. The formazan crystals formed were solubilized in DMSO, and the plates were analysed at 570 and 650 nm using a SpectraMax Paradigm multi-mode microplate reader (Molecular Devices). As a positive control for cytotoxicity, 10% DMSO was used, and as a negative control, 10% PBS was applied.

Cell lysates and dot-blot assay

Cells were cultivated in 25 cm^2 flasks and treated for 48 hours with soluble rPrP or aggregated rPrP:N2aRNA (1:5 ratio) at 0.71 µM. After treatment, cells were washed three times with PBS and lysed using liquid nitrogen in a lysis buffer (10 mM Tris-HCl pH 7.5, 150 mM NaCl, 1 mM EDTA, and 1% Triton X-100 supplemented with a protease inhibitor cocktail, Sigma-Aldrich, USA). Then, samples were centrifuged at 300 *g* for 5 min. The protein content was quantified using the Lowry assay [33] and stored at – 80 °C. For dot-blot assays, 10 µg of protein lysates were applied to a nitrocellulose membrane, which was blocked with 1% casein blocking buffer for 1 hour at 4 °C and incubated overnight at 4 °C with the primary antibody A11 (1:5,000 dilution) (Millipore). The membranes were washed five times with TBS-T, incubated with goat anti-rabbit secondary antibody (1:10,000) at room temperature for 1 h, washed 3 times with TBS-T and twice with TBS. The analysis was performed using the Clarity™ Western ECL Substrate kit (Bio-Rad Laboratories, EUA) and images were obtained in a ChemiDoc MP Basic Imaging System (Bio-Rad Laboratories, EUA). Densitometry of the dots was quantified using the ImageJ software (version 1.43 r, National Institutes of Health) and normalized against the control, which was set to 1 [34].

Sequencing of RNA molecules isolated from rPrP:RNA aggregates

RNA sequencing was performed at LaCTAD (Central Laboratory of High-Performance Technologies, UNICAMP, Campinas, Brazil) using a HiSeq2000 (Illumina, paired-end, 2 × 100bp) with three replicates for each condition, as follows: *i*, input total N2aRNA; *ii*, RNA extracted from aggregates with no treatment; *iii*, RNA extracted from aggregates and washed with 250 mM NaCl; *iv*, RNA extracted from aggregates and washed with 350 mM NaCl; *v*, RNA extracted from aggregates and treated with RNase A (see Figure 1); for a total of 15 samples. The Illumina kit TruSeq RNA Library Prep Kit v2 was used to generate the RNA-seq libraries for sequencing, omitting the poly-A tail capture step, to assess the entire transcriptome. Table S2 presents the total number of reads obtained from each sample and the number of high-quality reads passing the standard Illumina quality filters.

Bioinformatic analysis

Quality control of reads was performed using FastQC (v.0.11.7) [35]. To filter low-quality reads and trimming adapters we used Fastp (v0.20.0) [36]. Mycoplasma contamination was assessed using 12 different mycoplasma genomes retrieved from the NCBI repository. Bowtie2 (v2.2.9) [37] was used with default parameters to align the reads to 12 different mycoplasma genomes. These organisms were selected based on MycoStrip™ (Mycoplasma Detection Kit, InvivoGen) which includes six species of mycoplasma representing about 95% of cell culture contamination. The reads were aligned as unpaired, thus any mapped read R1 or R2 that mapped to any mycoplasma organisms had its pair discarded from further analyses. SeqKit (v 2.2.0) [38] was used to filter out reads that mapped to any mycoplasma organisms using the grep -vf option (see Fig. S1 and S2, Table S3 and supplementary file for details).

The remaining reads were mapped to the mouse genome using mm39 primary assembly (Mus_musculus.GRCm39.dna.primary_assembly.fa) and the reference transcriptome from Ensembl version 106 (Mus_musculus.GRCmm39.106.chr.gtf) using STAR (v2.7.0c) [39] with 2-step mode and ENCODE parameters. DNA contamination was checked using the QualiMap (v2.2.1) algorithm [40]. To identify RNAs enriched in each assay, we performed two different analyses, one using an RNA-seq-like analysis pipeline, and the other using ChIP-seq-like enrichment analysis methods, as follows. In the RNA-

seq-like analysis, quantification was performed using RSEM (v1.3.0) [41] and the significant differential abundance analysis was conducted with voom + weights [42], using batch as covariable in the model, comparing each group to control (input). For the ChIP-seq-like analysis, we mapped the reads against the mm39 transcriptome from Ensembl version 106 using STAR with the output option – quantMode TranscriptomeSAM. Quality mapping was checked using QualiMap (v.2.2.1) [40]. To keep the properly paired reads, we used SAMtools (v1.8) [43] with flags -f 0 × 2and -F 4, and the fixmate and markdup options were used to exclude PCR duplication reads from further analyses. MACS2 (v 2.1.0) [44,45] was used to call significantly enriched peaks in broad mode, with the input of each batch serving as a control.

Enrichment analysis

Gene Ontology (GO) enrichment was performed using WebGestalt [46], using ensembl_geneid as the identifier type. The Over-Representation Analysis (ORA) was selected with functional non-redundant databases of Biological Process (BP), Cellular Component (CC) and Molecular Function (MF). In the advanced parameters, we set the minimum number of genes per category to 2 and applied a false discovery rate (FDR) threshold of ≤ 0.05.

Genome browser tracks

The tracks are available at https://verjo101.butantan.gov.br/users/papers/yraima/ in BigWig format. To upload tracks, use My Data > Custom Tracks in the UCSC Genome Browser [47] using the mm39 assembly. To merge uploaded tracks, use My Data > Track Collection Builder.

Motif enrichment analysis

Motif enrichment analysis was performed using MEME (v. 5. 4.1) [48,49]. First, the Markov background model was built using the mouse transcriptome, considering only transcripts expressed in N2aRNA with the option -m 1. The enrichment analysis was performed using the FASTA file from 53 regions of 36 transcripts, with the background file represented by the Markov background model. The following parameters were used: -rna -minwidth 5 -maxwidth 20 -mod anr -evt 0.05.

RNA structure analysis

The RNA structure analysis was performed with the mxfold2 algorithm [50], using the 'predict' function with default parameters, previously trained by the authors. The similarity score (SS) was calculated with RNAsmc (v. 0.8.0, R package) [51], and the range of values is 0 to 10, indicating the lowest to the highest similarity. The set of miRNAs was randomly selected from the ENCODE annotation (60 sequences), and the 5S_rRNA set was filtered to 100–120 nt and selected from the ENCODE annotation (31 sequences). The 400 highly confident tRNA coordinates (*Mus musculus*) were downloaded from GtRNAdb [52], and then 60 sequences were randomly chosen.

Statistical analysis

The analysis was performed using GraphPad Prism 8.1.1. For the aggregation assay, a one-way ANOVA Bonferroni multiple comparisons test was used to determine significant differences between the input (rPrP + N2aRNA before re-extraction) and the rPrP + N2aRNA re-extracted (*p-value <0.05 and **p-value <0.01). Data are presented as means of replicates, and the error bars represent the standard deviation. For the turbidity assays, one-way ANOVA followed by Tukey's post-hoc test was used for statistical analysis (****p-value <0.0001). Data are presented as mean ± SD. Additionally, quantification of droplets and measurement of their area (μm^2) were performed under the conditions rPrP:N2aRNA (2:1) and rPrP:N2aRNA (1:5). Statistical analysis was conducted using an unpaired parametric t-test (****p-value <0.0001, ***p-value <0.001). Data are presented as the mean of replicates, with error bars representing the standard deviation.

Results

rPrP phase separation and aggregation induced by N2aRNA are dependent on the rPrP:RNA stoichiometry

As previously described, the N2aRNA extract can induce rPrP aggregation, altering its secondary structure content and yielding species that are partially resistant to proteinase K digestion and toxic to cultured neuroblastoma cells [14]. To confirm this data, rPrP was incubated with the total RNA extract (N2aRNA), and both turbidity (400 nm) (Fig. S3A) and light scattering (320 nm) (Fig. S3B) values were collected. As expected, the addition of the N2aRNA extract at a 2:1 rPrP:RNA ratio (μg/mL) induced a significant increase in turbidity and light scattering (Fig. S3).

The protein:NA stoichiometry is crucial in determining whether phase separation or aggregation occurs, with higher protein to NA ratios facilitating LLPS [26,27,53]. Thus, we conducted turbidity assays at different rPrP:RNA stoichiometries (2:1 and 1:5) and characterized the final species by optical and transmission electron microscopy (Figure 2). We found that at the higher rPrP:RNA ratio (2:1) (Figure 2(A)), LLPS occurred without the formation of insoluble aggregates (Figure 2(C), top row); in contrast, when the N2aRNA concentration was increased (1:5 rPrP:RNA ratio) (Figure 2(B)), aggregation was observed with negligible LLPS (Figure 2(C), bottom row). These data corroborate the re-entrant behaviour of NA-induced LLPS in PrP [27,54]. The quantification of droplets (Figure 2(D)) revealed a significant difference in their number, with a substantial increase in the 2:1 condition compared to the 1:5 condition, where condensates were drastically reduced. Analysis of droplet area (Figure 2(E)) did not indicate significant differences between conditions; however, in the 2:1 condition, variability in droplet size was more pronounced, likely due to dynamic coalescence, a characteristic feature of LLPS systems [23]. Droplets exhibited dynamic behaviour, as expected in liquid-liquid phase separation systems [23], reinforcing the fluidity and fusion of condensates observed in the 2:1 condition.

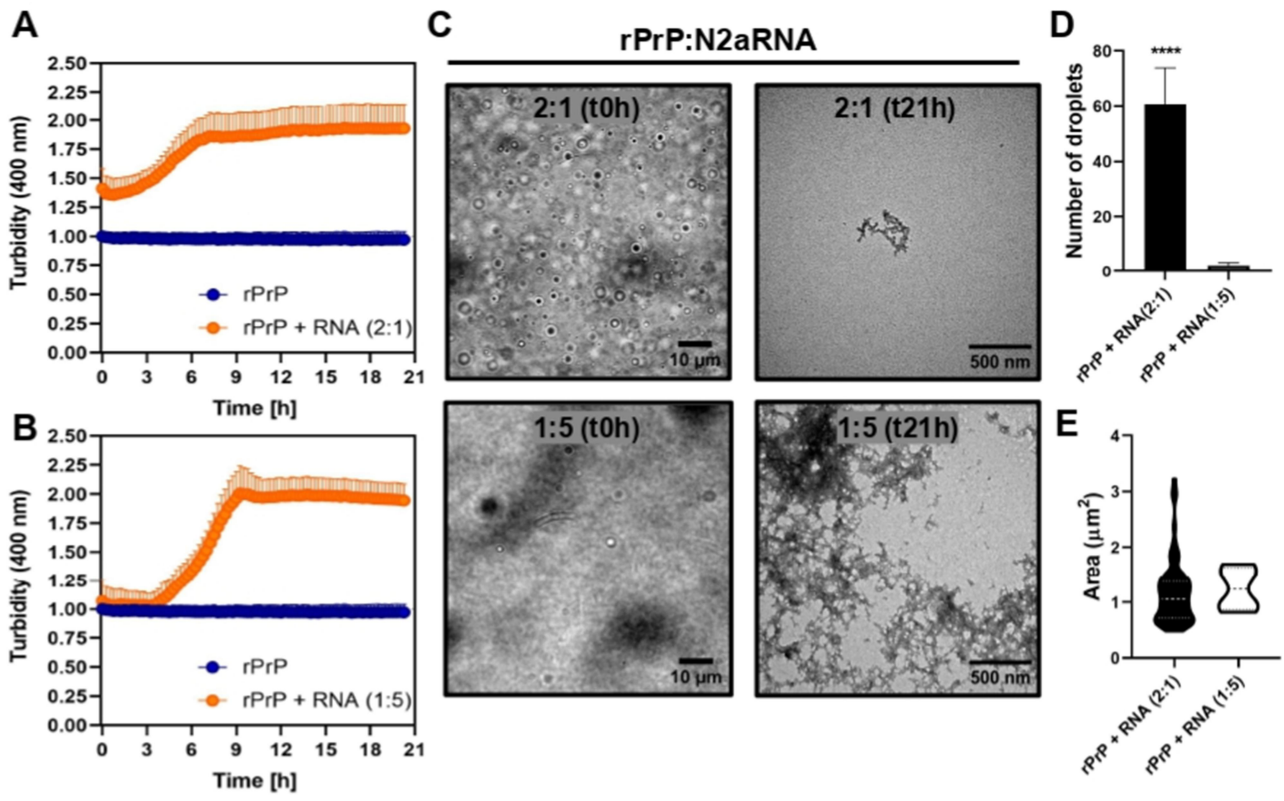

Figure 2. N2aRNA induces LLPS and aggregation of rPrP at different stoichiometries. (A) Turbidity of rPrP alone (blue circles) and in the presence of N2aRNA at a 2:1 stoichiometry (orange circles) measured over 21 hours. (B) Turbidity of rPrP alone (blue circles) and with N2aRNA at a 1:5 stoichiometry (orange circles) measured over 21 hours. (C) Optical microscopy images and transmission electron microscopy (TEM) images of rPrP + N2aRNA at 2:1 (top row) and 1:5 (bottom row) stoichiometries, showing LLPS droplets at $t = 0$ h and the formation of aggregates at $t = 21$ h. The images are representative of 10 independent fields. (D) Quantification of the number of liquid droplets in rPrP + N2aRNA samples at 2:1 and 1:5 stoichiometries. A significant increase in the number of droplets was observed in the 2:1 condition compared to 1:5, where condensates were drastically reduced. (E) Droplet area distribution in rPrP + N2aRNA samples at 2:1 and 1:5 stoichiometries. Statistical analysis was conducted using an unpaired parametric *t*-test for D and E panels (****p-value <0.0001, $N = 8$). Data are presented as means of replicates, with error bars representing the standard deviation. rPrP concentration in turbidimetry assays was 115 µg/mL, and in microscopy images, 230 µg/mL.

Transmission electron microscopy revealed the formation of organized branched aggregates upon incubation with the RNA input at the 1:5 rPrP:RNA ratio (Figure 2(C), bottom row). To verify whether these aggregates were cytotoxic, a cell viability assay (MTT reduction) was employed. There was a significant increase in the cytotoxic effect of the N2aRNA-induced rPrP aggregates on N2a cells when compared to rPrP at the same concentration (2.5 µM) (Figure 3(A)). Cells were treated with the samples for 72 hours and we observed that this effect was concentration-dependent (Fig. S4).

To verify whether the RNA-induced rPrP aggregates could convert native PrP^C into misfolded, aggregated species, as occurs in prion diseases, we performed a dot-blot assay with A11, an antibody that is specific for prefibrillar oligomeric species [55]. We selected a concentration for the rPrP:N2aRNA (1:5 ratio) samples where cytotoxicity was ~ 50% (0.7 µM) (Fig. S4) and treated cells with either rPrP:N2aRNA or unbound rPrP for 48 h. Then, 75% of the cells were collected for lysate preparation and fresh medium was added to the flask. When ~ 80% confluency was reached again, cells were harvested for another lysate (Figure 3(B), second passage). These lysates were analysed for their amyloid nature with A11 antibody, and a tenfold increase was observed for the cells treated with the rPrP:N2aRNA (1:5) aggregates when compared to the control N2a cell lysate (Figure 3(B)). Another interesting feature is that when cells were harvested and grown to confluence again, the amyloid oligomer pattern observed in the first passage was retained, indicating the seeding capacity of PrP aggregates and leading to their amplification in the growing cells (Figure 3(B)). These results suggest that upon incubation with N2aRNA, rPrP acquires scrapie-like properties, becoming able to catalyse the aggregation of PrP^C from the host (in this case, from the N2a cells). These findings, however, warrant future investigation.

To investigate the specificity of the RNA interaction with PrP and its resulting effects, we performed turbidity assays using α-synuclein and a 25-mer DNA aptamer (A1_mut) as controls. α-synuclein, which forms amyloid aggregates in Parkinson's disease [56], did not undergo phase separation or form aggregates upon incubation with N2aRNA at the two protein:NA ratios (2:1 and 1:5) (Fig. S5A). In contrast, a DNA aptamer (A1_mut), previously shown to induce liquid-to-solid transition of the globular domain of PrP ($PrP^{90–231}$) [27], induced formation of liquid droplets under both conditions but did not induce rPrP aggregation (Fig. S5B). These results suggest that the RNA-rPrP interaction exhibits specificity, as LLPS was observed at a 2:1 stoichiometry, whereas

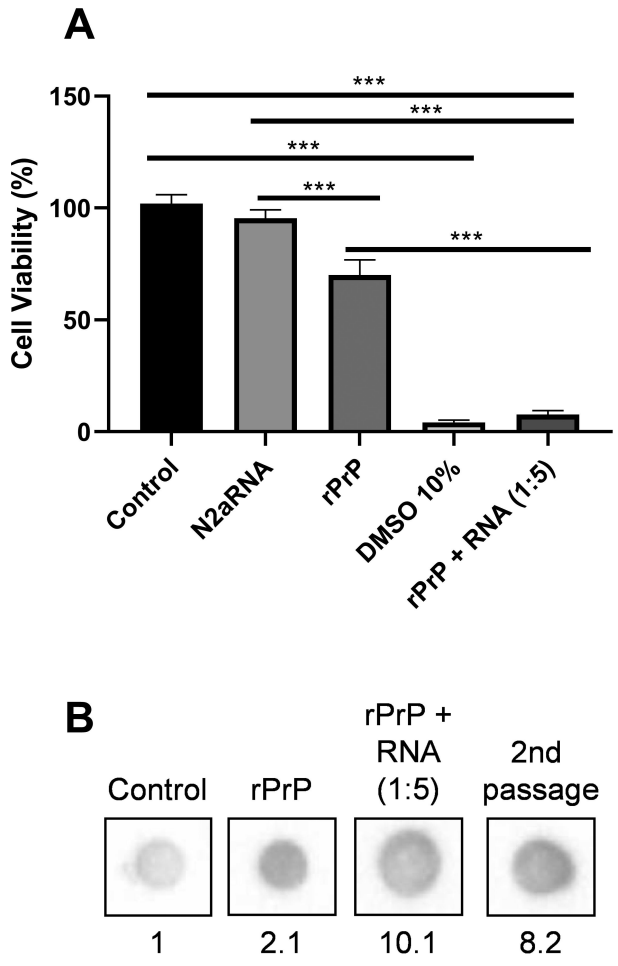

Figure 3. N2aRNA-induced rPrP aggregates are cytotoxic and exhibit amyloid characteristics. (A) MTT assay showing that rPrP + RNA (1:5) aggregates are cytotoxic to Neuro2a cells. Final concentrations in the wells: 0.0115 mg/mL rPrP and 0.0575 mg/mL N2aRNA. As a positive control for cytotoxicity, 10% DMSO was used, while 10% PBS served as the negative control. Statistical analysis was performed using one-way ANOVA with pairwise multiple comparisons using the holm-sidak method (***p-value <0.001). (B) Dot blot assay with A11 antibody. N2a cells were treated with 0.7 µM of either the soluble rPrP or the rPrP+RNA (1:5) aggregates. Cells were grown to 80% confluency. Then, cells were harvested and lysed. The remaining rPrP:N2aRNA-treated cells were subcultivated and lysed after reaching the same confluency. Cell lysates were quantified, and 10 µg of each lysate was submitted to dot blot with the anti-amyloid oligomers antibody A11. The number below each dot-blot indicates the increase in A11 labelling when compared to the control N2a cells lysate.

a 1:5 ratio led to aggregation without phase separation (Figure 2). This behaviour was not replicated by the tested controls, indicating that the interaction of PrP with RNA follows a distinct mechanistic pathway that depends on RNA concentration and differs from interactions with other nucleic acids.

Recovered RNA preserves the effects on rPrP phase separation and aggregation

We next asked which molecules in the RNA extract would preferentially interact with rPrP and be responsible for aggregation and/or phase separation.

Two strategies were developed to recover rPrP-bound RNA and identify which RNA molecules from the N2aRNA extract bind rPrP with high affinity. Figure 1 illustrates the two different protocols used in this work. In the first protocol, we washed the aggregates with 250 mM NaCl (step 4b in Figure 1) or 350 mM NaCl (step 4c in Figure 1) to remove weakly bound RNA (non-specific binding). In the second protocol, we treated the aggregates with RNase A for 1 h at 37 °C (step 4d in Figure 1) to isolate the sequences that interacted most tightly with rPrP, thus being retained within the insoluble species and protected from RNase A digestion. After the treatments, the RNAs that remained bound to rPrP were recovered with TRIzol extraction. Three batches of RNA samples for each protocol were prepared using the strategy described above. The size distribution of the RNAs recovered from these treatments in all batches was evaluated by agarose gel electrophoresis. In all samples, it was possible to visualize bands corresponding to ribosomal RNA subunits (Fig. S6). Recovered RNA after the different treatments was able to increase turbidity in an rPrP solution (Fig. S7), indicating formation of PrP condensates.

As the rPrP-bound RNA recovered after digestion with RNase A (Figure 1) yielded a significant increase in turbidity (Fig. S7), we performed the subsequent experiments with the RNase-treated sample only and compared with the input (N2aRNA). The RNAs present in the RNase-treated sample triggered rPrP phase separation at the 2:1 (rPrP:RNA) ratio, but no aggregated species were observed (Figure 4). Additionally, the addition of 500 mM NaCl led to the dissolution of LLPS droplets (Figure 4(B)), indicating that electrostatic interactions play a key role in the phase separation process, as commonly observed in LLPS systems [24]. Consistently, the droplets exhibited dynamic behaviour, further reinforcing the reversible nature of this phase separation. It is interesting to note that the analysis of droplet number showed a significant increase in the rPrP + RNase-treated RNA condition compared to the untreated condition (2:1) (Figure 4(C)), and the droplet area also increased significantly (Figure 4(D)). We can conclude that at least part of the RNAs responsible for PrP phase separation was preserved after treatment with RNase A, suggesting that an RNA population with high affinity for PrP was indeed selected.

Recovered RNA sequencing and analysis

rPrP aggregation was conducted in the presence of RNA molecules in biological triplicate. We used either (A) 250 mM NaCl or (B) 350 mM NaCl to purify the sequences more avidly bound to PrP, or (C) RNase A to perform a more stringent purification of RNAs bound to PrP. Recovered RNA quantification is summarized in Table S1.

For each experiment, RNAs that remained bound to aggregated rPrP after washes were paired-end sequenced in an Illumina HiSeq2000 instrument to produce 12 RNA-seq datasets. These datasets consist of 3 replicates for each of four different conditions (Figure 1; 4a, RNA extracted from aggregates with no treatment; 4b, RNA extracted from aggregates washed with 250 mM NaCl; 4c, RNA extracted from aggregates washed with 350 mM NaCl; and 4d, RNA extracted from aggregates treated with RNase A). In addition, input total N2aRNA (three replicates before incubation with rPrP) was also sequenced, resulting in a total of

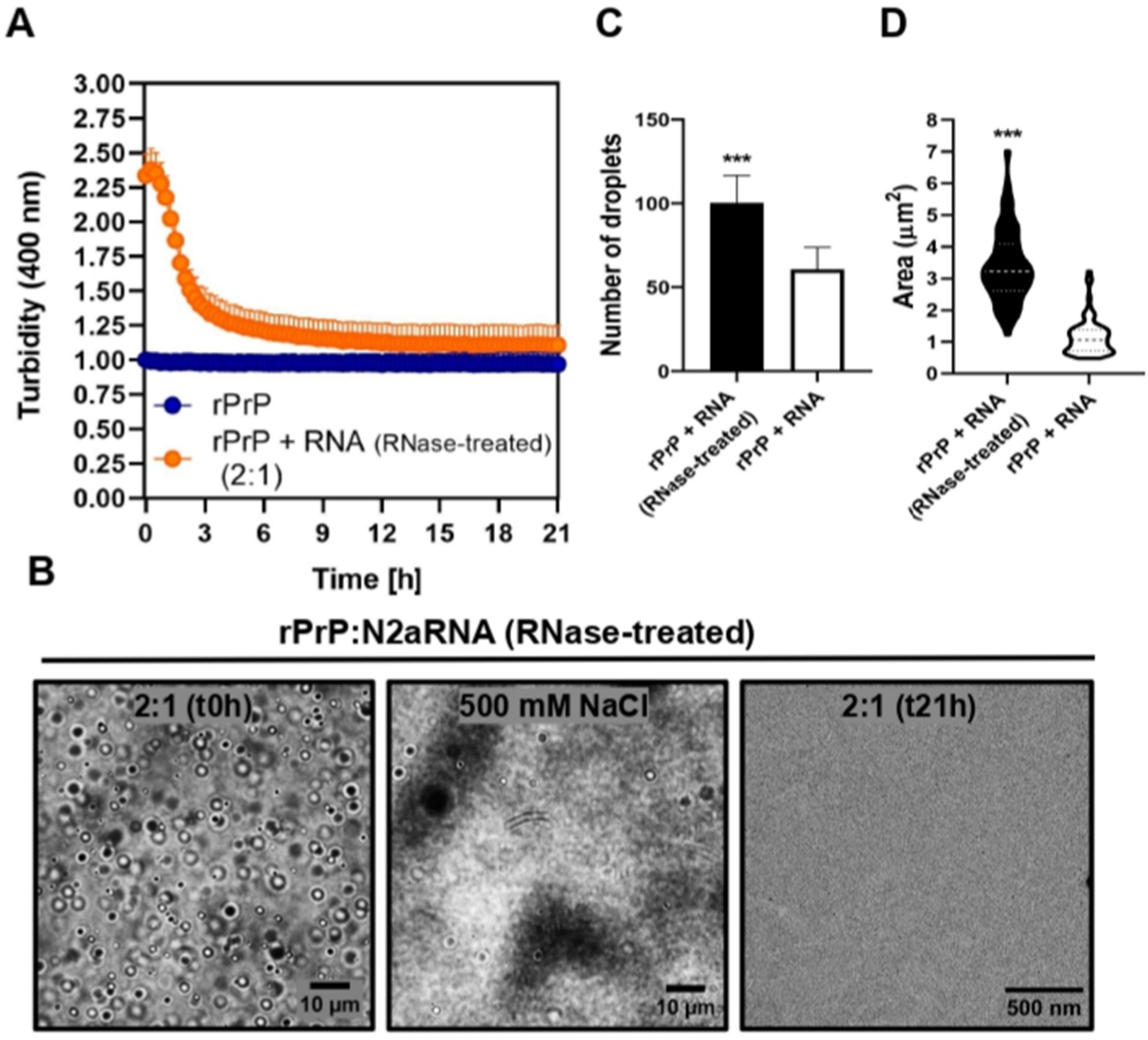

Figure 4. N2aRNA re-extracted after RNase treatment induces LLPS of rPrP. N2aRNA was incubated with rPrP at a 2:1 stoichiometry for 10 minutes, followed by RNase treatment to isolate the N2aRNA. The re-extracted N2aRNA was then incubated with rPrP at the same stoichiometry (2:1), and turbidity was monitored over time. (A) Turbidity of rPrP alone (blue circles) and in the presence of re-extracted N2aRNA at 2:1 stoichiometry (orange circles) measured over 21 hours. The re-extracted N2aRNA induced a ~ 133% increase in turbidity compared to rPrP alone. Turbidity values were normalized by dividing all measurements by the mean absorbance of rPrP alone at the first time point. (B) Left: optical microscopy of rPrP + re-extracted N2aRNA (2:1), revealing the formation of LLPS droplets. Middle: addition of 500 mM NaCl disrupted the LLPS droplets, demonstrating the salt sensitivity of the system. Right: transmission electron microscopy (TEM) image of rPrP + re-extracted N2aRNA (2:1) highlighting the absence of aggregates. (C) Quantification of the number of droplets formed in rPrP + RNA samples (2:1 stoichiometry) treated with RNase compared to untreated samples. A significant increase in droplet formation was observed in the RNase-treated condition compared to the untreated condition. (D) Droplet area distribution under the same experimental conditions. Droplets formed in the RNase-treated condition exhibited significantly larger areas than those in the untreated condition. (C and D), statistical analysis was conducted using an unpaired parametric *t*-test (***p-value <0.001, $N = 8$). Data are presented as means of replicates, with error bars representing the standard deviation. The images are representative of 10 independent fields. rPrP concentration in turbidimetry assays was 115 μg/mL, and in microscopy images, 230 μg/mL.

15 RNA-seq datasets. All sequenced reads were aligned to the mm39 version of the mouse genome using STAR [39]. The total number of sequences obtained and the number of sequences that mapped to the mouse genome in each of the samples is shown in Table S2. Since genomic DNA can interfere in rPrP aggregation, we investigated whether genomic DNA possibly present in our samples was associated with protein aggregation. For this, we used the quantification of reads mapping to intergenic regions in the mouse genome as a proxy of DNA contamination; intronic regions were not accounted for because sequencing of total RNA without poly-A selection tends to capture unprocessed RNAs as well as processed spliced ones [57]. No significant association was found between genomic DNA and protein aggregation (see supplementary file). Notably, most of the reads were mapped to ribosomal RNAs (about 62.67%) due to the strategy of sequencing total RNA, which was implemented by the library construction approach that was used.

rPrP-bound sequences matching different RNA molecules related to the ribosomal complex

To investigate RNA molecules bound to rPrP, we used four subsample datasets, each composed of 3,000,456 reads randomly picked from each of the 15 samples, and for each

subsample dataset we performed enrichment analyses using two different approaches, one based on RNA-seq and the other on ChIP-seq pipelines (Fig. S8). The RNA-seq pipeline aimed to identify and characterize quantitative differences in RNA abundance between biological samples from two or more groups, an RNA-seq-like approach [58]. While the nucleotide binding protein motif-enrichment identification pipeline, adapted from the ChIP-seq method, was used to identify DNA binding sites for a protein of interest [58,59], and this was a ChIP-seq-like approach. We focused on the RNase A assay due to the higher percentage of rPrP aggregation. For the RNA-seq-like analysis pipeline, nine RNA molecules were identified as enriched after RNase A treatment compared with total N2aRNA. We applied differential expression analysis to the four subsampled datasets, resulting in a mean value of 36 differentially expressed transcripts (Table 1, FDR ≤ 5%). As our interest was in the enriched RNA molecules, we selected only 'upregulated' genes, resulting in 37 transcripts, and only 10 (27%) were identified in at least three subsampled datasets analyses or more (Figure 5). Applying the same rationale, we conducted the ChIP-seq-like analyses on the four subsampled datasets, utilizing total N2aRNA as input for each group comparison. It is noteworthy that RNase A treatment yielded a higher number of peaks compared to any other group (Figure 6A and Table 2, q-value ≤5%), and exhibited the highest degree of overlapping peaks among replicates (Figure 6B and Table 2). Therefore, our focus was directed towards the RNase A assay results. Peaks identified in at least two replicates were considered for further analysis and resulted in 77 peaks on average (belonging to 26 transcripts). Transcripts that were identified in at least two different datasets were selected and resulted in 36 transcripts representing 34 genes (Figure 6C) summarized in 53 non-redundant merged regions. The GO enrichment analysis (FDR <5%, Cellular Component) showed the Ribosome (GO:0005840) category as overrepresented with 17 genes (*Rps20, Rps17, Rps15a, Rps12, Rplp0, Rpl13, Rpl11, Eef1a1, Rps27a, Rps23, Rpl7, Rpl5, Rpl32, Rps4×, Rps15, Rpl31, Rpl23a*) along with other 4 GOs named preribosome (GO:0030684), polysome (GO:0005844), protein folding chaperone complex (GO:0101031) and myelin sheath (GO:0043209) (Figure 6D, Table S4). Comparing the results obtained with the RNA-seq-like and ChIP-seq-like approaches, both analyses identified eight genes in common whose RNAs were bound to rPrP: *Rn7S1* (7S RNA 1), *Rn7S2* (7S RNA 2), *Rps4x* (ribosomal protein S4, X-linked), *Rps15a* (ribosomal protein S15A), *Rps27a* (ribosomal protein S27A), *Rpl11* (ribosomal protein L11), *Rpl13* (ribosomal protein L13) and *Hspa8* (heat shock protein 8). The abundance of reads mapped along the locus of each of the three selected genes is shown by snapshot images of the genome browser (Figure 7A-C). Curiously, the density of mapped reads along the entire locus of the *Rps4x* gene indicates that the unspliced immature mRNA of *Rps4x* was bound to PrP (Figure 7C). 7S RNAs are abundant non-coding cytosolic/mitochondrial polyadenylated RNAs predicted to regulate transcription initiation in mammalian mitochondria [60]. *Rn7S1* and *Rn7S2* (Figure 7A,B) are composed of 300 nucleotides, with > 60% GC content. *Rps4x* (Figure 7C) encodes ribosomal protein S4, X-linked, a structural constituent of the ribosome predicted to enable RNA binding activity.

Table 1. Differentially expressed RNAs (DEGs) with FDR ≤ 5% comparing RNase a assay versus input N2aRNA.

Analysis	DEGs (FDR ≤5%)	Up	Down
Dataset-1	34	15	19
Dataset-2	37	18	19
Dataset-3	33	17	16
Dataset-4	40	17	23

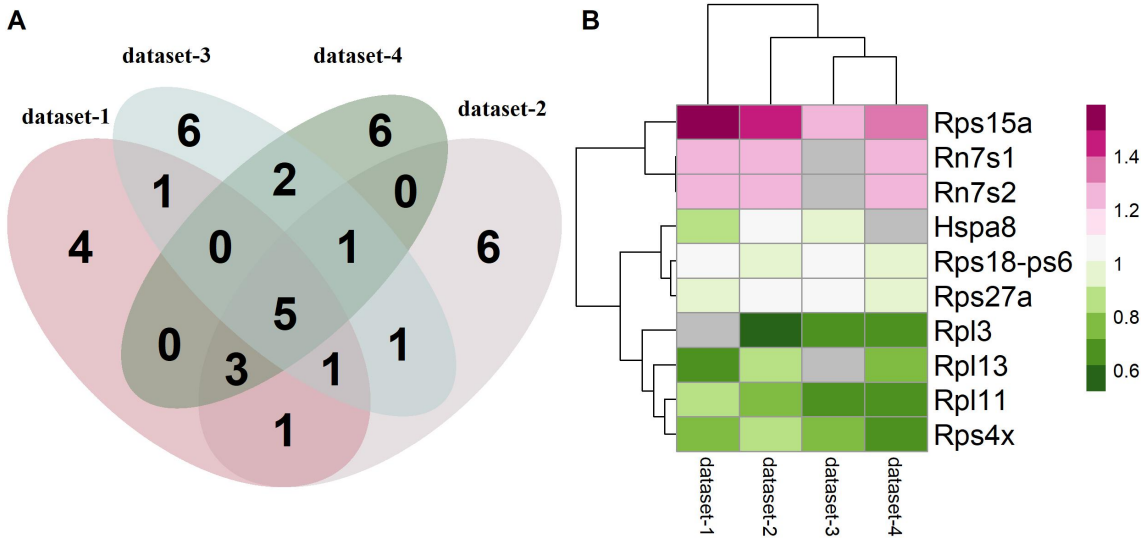

Figure 5. RNA molecules identified in rPrP aggregates/condensates. (A) Venn diagram of differentially expressed genes (DEGs) in each dataset analysis. (B) Heatmap of DEG analyses in each dataset. Columns represent each dataset analysis, and genes are shown in each row. Colors are scaled according to log2 Fold change (RNase A/N2aRNA total RNA).

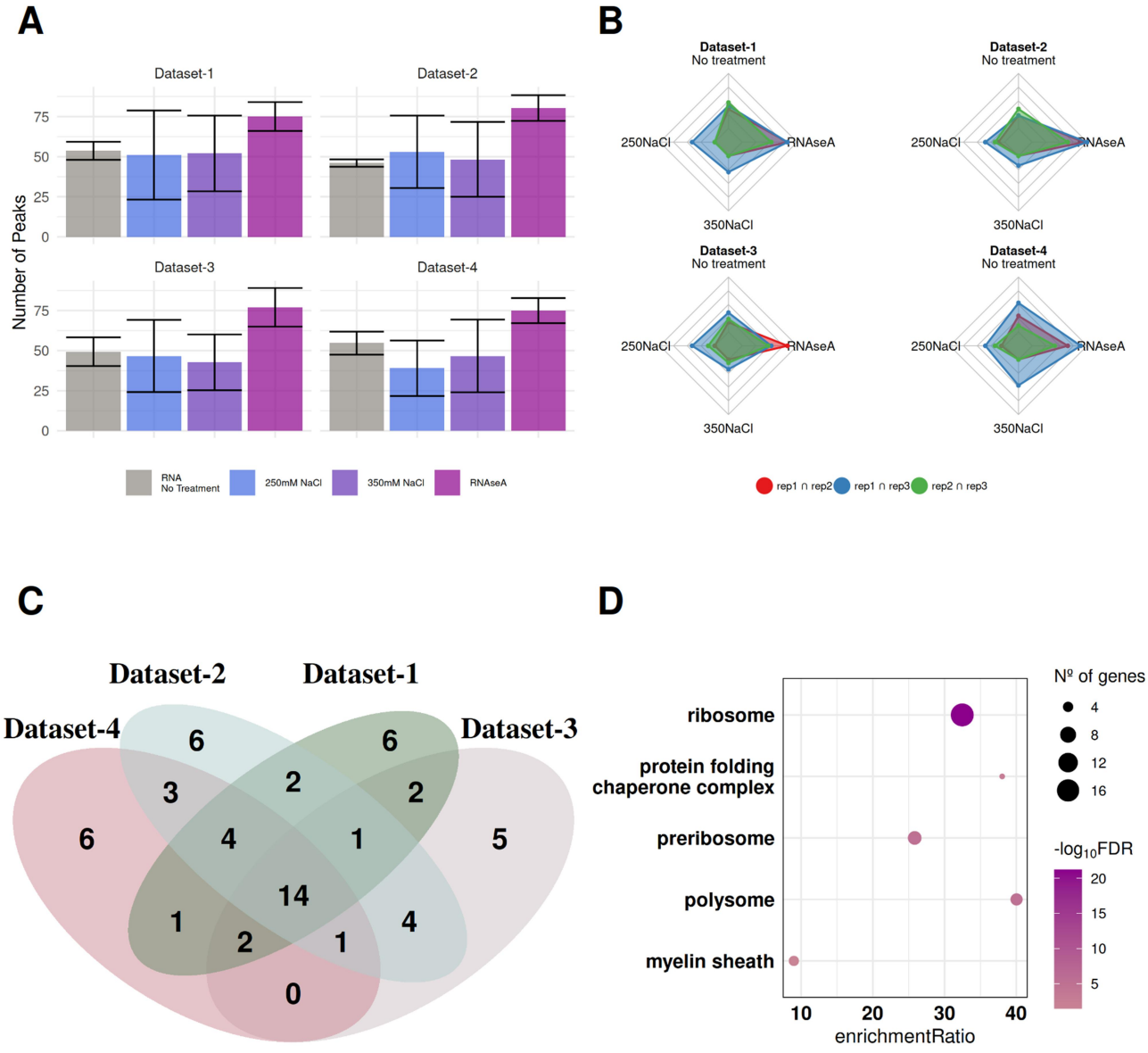

Figure 6. Regions of the RNA molecules bound to rPrP insoluble species. (A) Bar plot of the number of peaks in each dataset. Each group is represented on the x axis and coloured accordingly. The y axis shows the number of peaks identified. Error bars represent measurements from three replicates. (B) Radar plot of overlapping peaks among replicates. The number of overlapping peaks is shown in inner circles, and colours represent each intersection between two replicates. (C) Venn diagram of genes located at genomic coordinates under peak regions. (D) Gene ontology (GO) analysis of cellular component. The x-axis shows the enrichment ratio, and the y-axis shows the enriched categories. The size of the circles represents the number of genes identified, and colour reflects the -$\log_{10}$(FDR).

rPrP-bound RNAs are enriched in low complexity sequence motifs

To investigate the sequence motifs enriched in the rPrP-bound RNAs, we used 53 non-redundant regions from 36 transcripts that were identified in common in at least two different datasets from the ChIP-seq-like analysis. Among them, we found 3 enriched consensus motifs (E-value <0.05, Table 3). Among the motifs identified in different transcripts there were low complexity sequences (i.e. poly-U, poly-GA, Figure 8(A)). We predicted the RNA secondary structure encompassing these motifs (motif length + 10 nt up/downstream) using *mxfold2* as described in the Methods and calculated the structure similarities among them using the *RNAsmc* tool [51] and generated similarity scores (SS). A clustering analysis using the SS values showed that there were 3 main clusters of RNA structures (Figure 8(B)). Looking at the MEME motif types among the 3 clusters (Figure 8(B)) one can see that they are distributed along the RNA structural groups, indicating that the clusters are not entirely correlated with the sequence context since all MEME motifs are found in all 3 structural clusters (Figure 8(B)). To investigate the strength of these structural similarities, we compared them with the similarities found in 3 groups of highly structured RNAs: tRNA, miRNA and 5S_rRNA. The median of SS in intragroup comparison follows the order: tRNA (8.22), miRNA (7.03), MEME (6.98) and 5S_rRNA (6.19) (Figure 8(C)). The median of SS in intragroup comparisons are in general higher than when comparing SS between two different classes of RNAs (Figure 8(C)). To ensure that the SS value in MEME intragroup comparisons is not only due to its size (~40 nt), since the other classes show larger

Table 2. Number of peaks significantly identified in each group compared to the input N2aRNA (q-value ≤5%).

Groups	rep1	rep2	rep3	rep1 ∩ rep2	rep1 ∩ rep3	rep2 ∩ rep3	Dataset	No. of Genes
No treat.	62	43	56	6	7	8	1	13
	50	42	46	4	4	6	2	
	65	34	49	3	6	4	3	
	69	48	47	5	9	2	4	
250 mM	47	5	101	0	7	0	1	9
	79	8	72	2	6	3	2	
	59	3	78	0	7	2	3	
	50	5	62	1	6	3	4	
350 mM	66	6	84	0	5	0	1	4
	66	2	77	0	3	0	2	
	57	8	63	0	3	1	3	
	76	2	62	0	8	0	4	
RNaseA	84	84	57	14	14	9	1	34
	92	84	65	16	17	11	2	
	91	87	53	14	9	8	3	
	88	76	61	11	15	7	4	

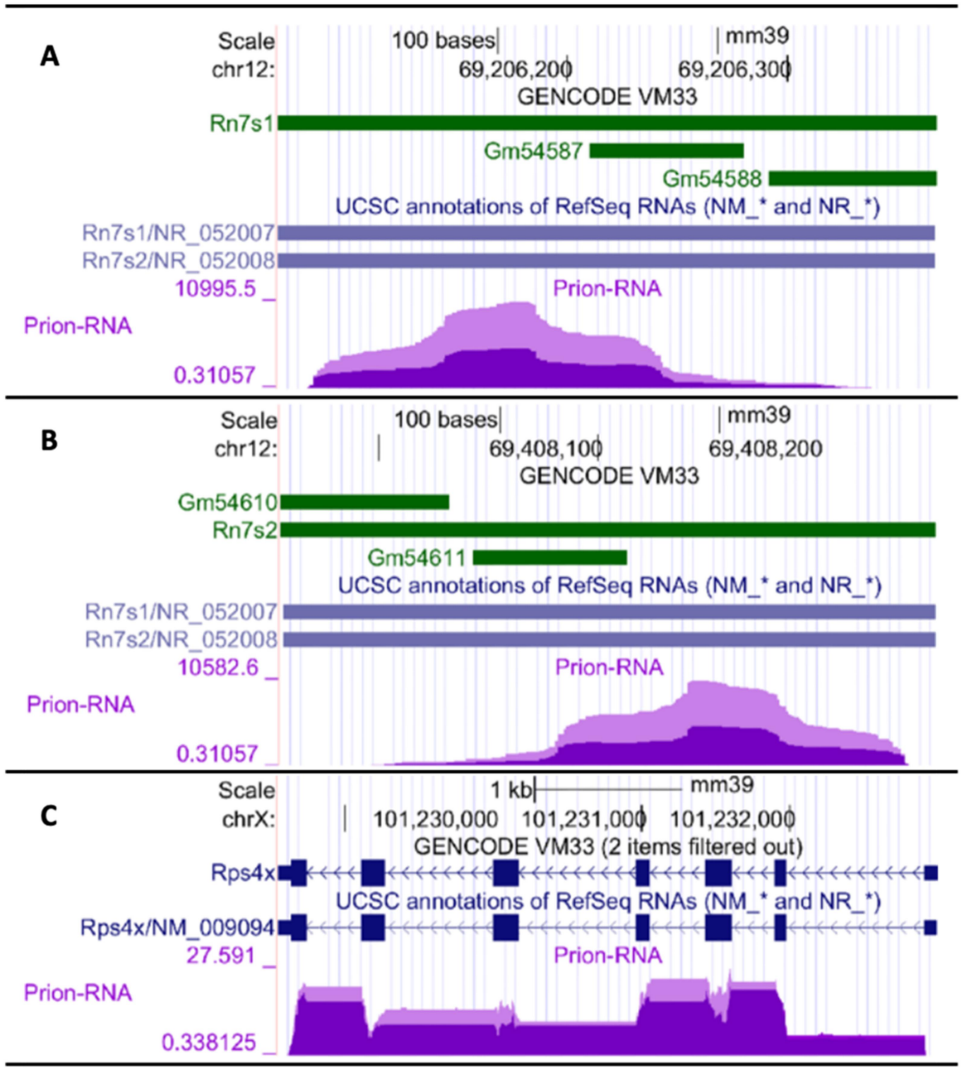

Figure 7. RNA molecules identified in both analyses. Genome browser visualization of three genes, shown in panels A to C, which were identified in common in both analyses' pipelines (RNA-seq-like and ChIP-seq-like). Genomic coordinates of each locus are shown at the top of each panel. GENCODE annotations of genes mapped to the locus are shown in the green tracks, and RefSeq annotations in the blue tracks. The 'Prion-RNA' track shows the abundance of RNA reads bound to rPrP in the RNase A-treated sample that mapped to this genomic region, indicated by light purple colour peaks. For comparison, reads from the total N2aRNA sample that mapped to this region are indicated by dark purple peaks.

Table 3. Enriched motifs among 36 transcripts bound to rPrP insoluble species (E-value ≤0.05).

Motif ID	Consensus motif sequence	Motif width (nt)	Enrichment E-values	# of unique motif sequences	# of target transcripts
MEME-1	YUYSYCAUWUUYCAYGUYYU	20	2.3e-072	24	2
MEME-2	GAGGAAGANRA	11	2.3e-010	57	23
MEME-3	UCMAUGUGCKDMCCUCCCG	19	6.4e-008	7	4

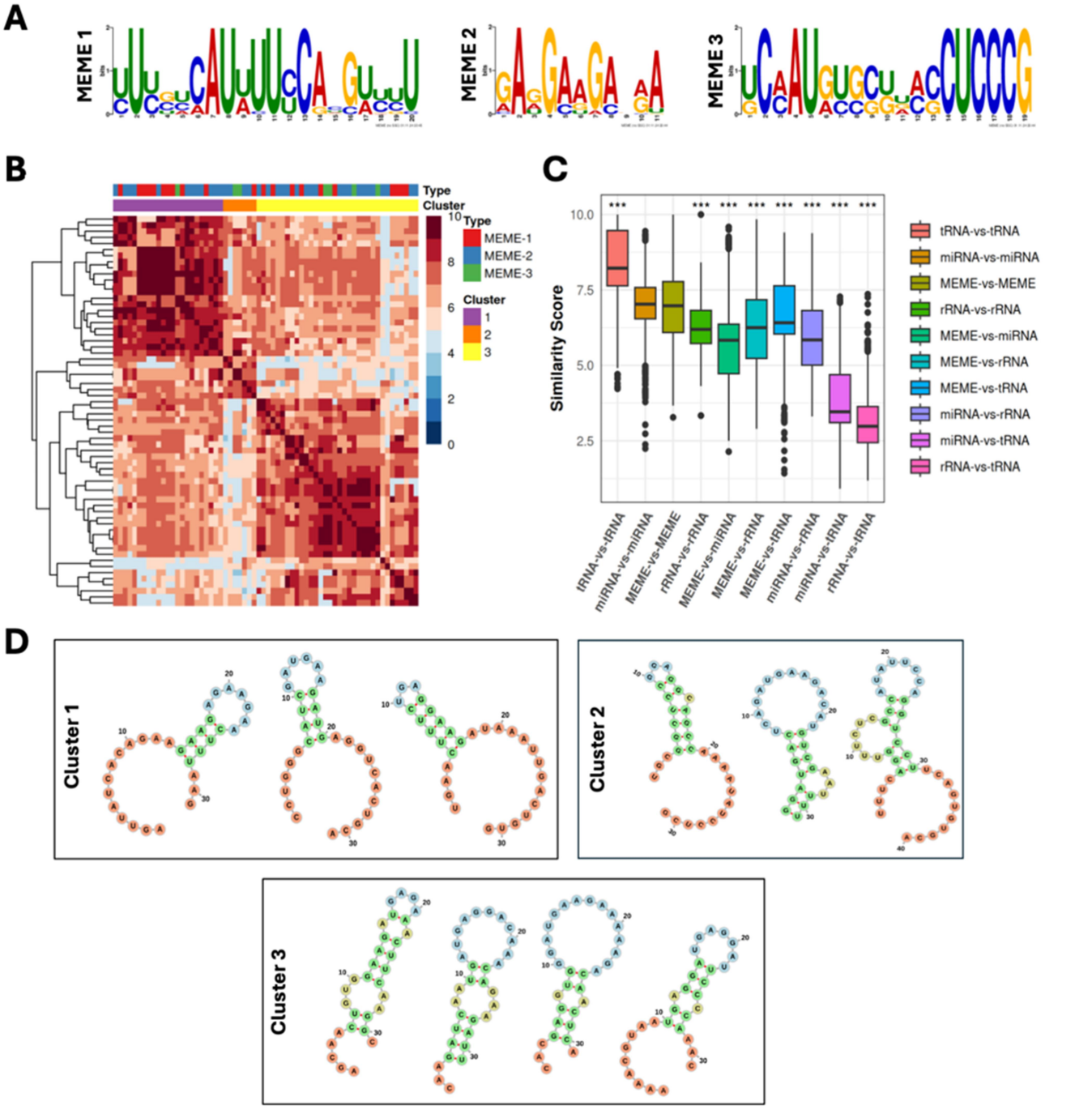

Figure 8. Enrichment motif analysis of RNA molecule regions bound to rPrP insoluble species. (A) Sequence motifs enriched in RNA molecules bound to rPrP. (B) Heatmap of similarity scores (SS); each row and column represent a sequence encompassing the motif (motif length + 10 nt upstream/downstream). The blue-to-red color scale reflects the low to high SS, respectively. (C) Boxplot of SS values among groups. The comparisons within and between groups are shown on the x-axis; the y-axis shows SS values. Significance is indicated by *** (*p*-value <1E–05) and was calculated between the MEME_MEME group vs each of the other groups. (D) Schematic representation of the representative structures formed by RNAs of the three structural clusters. Each cluster is outlined by a rectangle, and each short structural motif is represented by a different colour: hairpin loop (blue), stem (green), external loop (salmon), bulge loop and internal loops (gold).

RNAs with ~ 70 to 120 nt, we compared these MEME structures with other random sequences of the same length (40 nt) originated from the transcriptome and once again the SS of MEME intragroup was higher than the SS of random sequences (Fig. S9). The first structural cluster (Cluster-1) (Figure 8(D)) was composed of 23 sequences mainly formed by a hairpin loop (blue), stem (green) and external loop (salmon). Cluster-2 (Figure 8(D)) with 7 sequences had a similar structure, however with the presence of a bulge loop (gold) and Cluster-3 with 34 sequences showed a similar structure with an internal loop (gold) instead of a bulge loop (Figure 8(D)).

Discussion

Here, we identified a pool of RNA molecules involved in the ribosomal RNA complex preferentially bound to rPrP, using two different analysis approaches (RNA-seq-like and ChIP-Seq-like). Some RNAs were already reported to bind to rPrP to form aggregates, and a notable one is the 23S/28S rRNA [29]. In fact, rRNA is the most abundant type of RNA inside a living cell [61]. Based on this, it is no surprise that enriched rRNA-derived sequences would be found bound to rPrP. This finding is also supported by the fact that some molecules with high anti-prion activity *in vitro* and *in vivo*, such as guanabenz (GA) and 6-aminophenantridine (6AP), target rRNA [62,63]. These two compounds have no direct interaction with PrP and are not able to reduce PrP^{Sc} formation in cell free conversion assays but bind directly to rRNA [20].

Our findings are in line with the known fact that mammalian PrP interacts with ribonucleic acids and that these molecules could be involved in the early stages of prion diseases [30,64]. RNA molecules can stimulate PrP conversion into aggregates and induce formation of PrP^{Res} (PrP forms that are partially resistant to proteinase K digestion) *in* vitro [13,14,65]. Aggregates generated upon this interaction can be toxic to cultured mammalian cells [14] and have also been shown to induce prion disease in experimental animals [16]. Importantly, nucleic acids co-purify with scrapie-associated fibrils (SAF); RNA molecules extracted from SAF induced rPrP aggregation and caused prion-like disease in wild-type hamsters [16]. Recently, through an in-depth analysis of electron cryo-microscopy (cryo-EM) maps of brain-derived SAF, non-protein extra densities were observed within each fibril, attributed to RNA [19]. This evidence supports an *in vivo* interaction between PrP and biological polyanionic molecules, such as RNA.

Due to a partially efficient N-terminal signal peptide, part of the expressed PrP^{C} can be retained in the cytosol (reviewed in [66]; interestingly, it has been described that cytosolic PrP can participate in large ribonucleoprotein complexes, possibly stress granules, in the same cell line used here, N2a [67]. Stress granules are formed through liquid-liquid phase separation [68], which supports the role of specific RNAs to induce PrP phase separation *in vivo*. Among the components present in such granules, one can find RNA-binding proteins, and different types of RNA (mRNA, snU1RNA, 5S rRNA, miRNAs, and tRNAs) [69]. Here, we identified RNAs that encode several proteins involved in ribosomal complex; considering that cytosolic PrP is also engaged in aggresome formation, which includes RNA [69], it is valuable to further investigate the participation of nucleic acids in prion biology in diseased and healthy states (reviewed in [21,64,66].

Deregulation of RNAs encoding proteins involved in ribosomal complex was observed in ovine microglia with different permissive scrapie prion propagation [70] and siRNA assay of *Hspa13* in mouse neuroblastoma-derived cells reduced PrP^{Sc} positive cells [71]. Although these findings support that RNAs involved in ribosome complex can alter prion aggregation, at this point, it is not possible to determine whether these differences in prion aggregation and phase separation result from interactions occurring at different mRNA or protein levels.

Whether the length, conformation, or base composition of the RNA molecule is important to binding and induction of effects such as aggregation and toxicity is still a question to be answered. Here, we identified a set of RNAs with enriched motifs of widths from 11 up to 20 nucleotides, which suggest that these RNA motifs should be prioritized in future aggregation and phase separation experimental validation assays. In this context, analysis of RNAs extracted from brain infected material points to small fragments up to 55 nucleotides [16], but further investigation of the sequences is needed. The motifs identified here are mainly composed of low complexity sequences; interestingly, low concentrations of poly(U) formed complex with mutated human PrP (Y145Stop) [26], and poly(A) or poly(G) synthetic sequences restored PrP^{Sc} murine conversion [72], reinforcing the role of RNAs in prion replication.

Moreover, to investigate the potential of the identified motifs, we explored their secondary structure. Notably, the structures among the motif sequences were more similar to each other than to random sequences. Interestingly, our Cluster-1 structures resemble the secondary structure of nucleic acid aptamers screened against rPrP [27,73], SAF-93 (1–60), and A1. SAF-93 is an RNA aptamer selected as the minimal conformationally selective structure for PrP binding [73] and A1 is a single-stranded DNA aptamer that triggers rPrP LLPS [27]. This may lead to a putative mechanism by which RNAs could act and should be further investigated in the future.

In addition to protein aggregation modulated by nucleic acids (reviewed in [15,21,64], recent data highlight the role of NAs in liquid-liquid phase separation (LLPS) and liquid-to-solid transitions of proteins related to degenerative diseases, including PrP [27,53,64]. It has become clear that LLPS can precede non-functional protein aggregation [24,74] and we hypothesize that some of the identified RNA sequences might participate *in vivo* in PrP phase transitions. Here, we have observed that RNA-induced phase separation is dependent on the protein:NA ratio, in a re-entrant phase behaviour also seen for other neurodegenerative disease-related proteins [26,53]. We have previously characterized phase transitions of rPrP modulated by DNA aptamers *in vitro* [27], and showed that depending on the NA conformation, either formation of liquid droplets or solid species (aggregates) occurred. Now, we observe RNA-modulated LLPS and aggregation in a (patho)

physiological relevant context that deserves further in-cell validation.

Finally, we speculate on potential in-cell PrP-NA roles. PrP may interact with the exosome complex, which is involved in the degradation of ribosomal RNAs. This could be a site for the catalytic action of rRNA in converting PrP^{C} to PrP^{Sc} [21], likely within a biomolecular condensate. This scenario would support a model where: *i*) the exosome complex and PrP are co-localized within a condensate/liquid droplet; *ii*) rRNA, possibly released from the degradation process, would act as a scaffold or catalytic entity facilitating the structural conversion of PrP; and *iii*) the concentrated environment of the condensate might enhance the interaction between PrP molecules, thereby promoting the formation of the pathogenic PrP^{Sc}. All these hypotheses should be interpreted with caution and undergo rigorous experimental validation.

Acknowledgments

We thank the National Center for Structural Biology and Bioimaging CENABIO, UFRJ, for the acquisition of TEM images and the Optical Tweezers Laboratory (LPO) (UFRJ) for optical microscopy imaging. We thank Dr. Patricia N. Fernandes (UFRJ) for the technical support, Dr. João Marques (UFMG) for inspiring discussions and Dr. Petar S. Kovachev (Uppsala University) for assistance with some graphics.

Disclosure statement

No potential conflict of interest was reported by the author(s).

Author contributions

CRediT: **Ana C. Tahira:** Conceptualization, Formal analysis, Investigation, Methodology, Visualization, Writing – review & editing; **Mariana P. B. Gomes:** Conceptualization, Formal analysis, Investigation, Methodology, Visualization, Writing – original draft, Writing – review & editing; **Maria Heloisa Freire:** Formal analysis, Investigation, Methodology, Visualization, Writing – review & editing; **Marcelly Muxfeldt:** Investigation, Methodology, Visualization; **Francisco Prosdocimi:** Formal analysis, Investigation, Methodology, Visualization, Writing – review & editing; **Yulli M. Passos:** Investigation; **Murilo Sena Amaral:** Investigation; **Leticia P. Felix Valadão:** Investigation; **Luciana P. Rangel:** Conceptualization, Formal analysis, Investigation, Methodology, Supervision, Visualization, Writing – review & editing; **Jerson L. Silva:** Conceptualization, Funding acquisition, Resources, Supervision; **Sergio Verjovski-Almeida:** Conceptualization, Funding acquisition, Project administration, Resources, Supervision, Writing – review & editing; **Yraima Cordeiro:** Conceptualization, Funding acquisition, Project administration, Resources, Supervision, Writing – original draft, Writing – review & editing.

Funding

This study was financed in part by the Coordenação de Aperfeiçoamento de Pessoal de Nível Superior - Brasil (CAPES) - Finance Code 001; by Fundação de Amparo à Pesquisa do Estado do Rio de Janeiro (FAPERJ); by the Conselho Nacional de Desenvolvimento Científico e Tecnológico (CNPq) ; by Fundação Butantan [FAPESP Grant 2018/23693–5].

Data availability statement

The genome browser tracks are available at https://verjo101.butantan.gov.br/users/papers/yraima/ bigwig format. The sequencing data records have been deposited in the Sequence Read Archive (SRA) under the BioProject number PRJNA1092090. Remaining data supporting the findings of this study are available within the article [and/or] its supplementary materials or upon request.

ORCID

Yraima Cordeiro http://orcid.org/0000-0003-4278-212X

References

[1] Prusiner SB. Prions. Proc Natl Acad Sci USA. 1998;95 (23):13363–13383. doi: 10.1073/pnas.95.23.13363
[2] Brettschneider J, Tredici KD, Lee V-Y, et al. Spreading of pathology in neurodegenerative diseases: a focus on human studies. Nat Rev Neurosci. 2015;16(2):109–120. doi: 10.1038/nrn3887
[3] Jucker M, Walker LC. Propagation and spread of pathogenic protein assemblies in neurodegenerative diseases. Nat Neurosci. 2018;21(10):1341–1349. doi: 10.1038/s41593-018-0238-6
[4] Caughey B, Baron GS, Chesebro B, et al. Getting a grip on prions: oligomers, amyloids, and pathological membrane interactions. Annu Rev Biochem [Internet]. 2009;78(1):177–204. Available from: http://www.ncbi.nlm.nih.gov/pubmed/19231987nhttp://www.pubmedcentral.nih.gov/articlerender.fcgi?artid=PMC2794486
[5] Caughey BW, Dong A, Bhat KS, et al. Secondary structure analysis of the scrapie-associated protein PrP 27–30 in water by infrared spectroscopy. Biochemistry. 1991;30(31):7672–7680. doi: 10.1021/bi00245a003
[6] Requena JR, Wille H. The Structure of the Infectious Prion Protein and Its Propagation. Progress in Molecular Biology and Translational Science. Elsevier Inc. 2017 150:341–359. doi:10.1016/bs.pmbts.2017.06.009
[7] Griffith JS. Self-replication and scrapie. Nature. 1967;215 (5105):1043–1044. doi: 10.1038/2151043a0
[8] Cordeiro Y, Machado F, Juliano L, et al. DNA converts cellular prion protein into the β-sheet conformation and inhibits prion peptide aggregation. J Biol Chem. 2001;276(52):49400–49409. doi: 10.1074/jbc.M106707200
[9] Abid K, Morales R, Soto C. Cellular factors implicated in prion replication. FEBS Lett. 2010;584(11):2409–2414. doi: 10.1016/j.febslet.2010.04.040
[10] Deleault NR, Harris BT, Rees JR, et al. Formation of native prions from minimal components in vitro. Proc Natl Acad Sci USA. 2007;104(23):9741–9746. doi: 10.1073/pnas.0702662104
[11] Supattapone S. Cofactor molecules: essential partners for infectious prions. Prog Mol Biol Transl Sci. 2020;175:53–75.
[12] Baskakov IV, Legname G, Prusiner SB, et al. Folding of prion protein to its native α-helical conformation is under kinetic control. J Biol Chem. 2001;276(23):19687–19690. doi: 10.1074/jbc.C100180200
[13] Silva JL, Gomes MPB, Tcrg V, et al. PrP interactions with nucleic acids and glycosaminoglycans in function and disease. Front Biosci. 2010;15(1):132–150. doi: 10.2741/3611
[14] Gomes MPB, Millen TA, Ferreira PS, et al. Prion protein complexed to N2a cellular RNAs through its N-terminal domain forms aggregates and is toxic to murine neuroblastoma cells. J Biol Chem. 2008;283(28):19616–19625. doi: 10.1074/jbc.M802102200
[15] Litberg TJ, Horowitz S. Roles of nucleic acids in protein folding, aggregation, and disease. ACS Chem Biol. 2024; 19(4):809–823. in press. doi: 10.1021/acschembio.3c00695
[16] Simoneau S, Thomzig A, Ruchoux M-M, et al. Synthetic scrapie infectivity: interaction between recombinant PrP and scrapie

brain-derived RNA. Virulence. 2015;6(2):132–144. doi: 10.4161/21505594.2014.989795
[17] Oesch B, Groth DF, Prusiner SB, et al. Search for a scrapie-specific nucleic acid: a progress report. Ciba Found Symp; 1988.
[18] Narang HK. Molecular cloning of single-stranded DNA purified from scrapie-infected hamster brain. Res Virol. 1993;144:375–387. doi: 10.1016/S0923-2516(06)80053-1
[19] Bridges LR. RNA as a component of scrapie fibrils. Sci Rep. 2024;14(1):5011. doi: 10.1038/s41598-024-55278-0
[20] Banerjee D, Sanyal S. Protein folding activity of the ribosome (PFAR) –– a target for antiprion compounds. Viruses. 2014;6(10):3907–3924. doi: 10.3390/v6103907
[21] Amaral MJ, Cordeiro Y. Intrinsic disorder and phase transitions: pieces in the puzzling role of the prion protein in health and disease [Internet]. In: Dancing protein clouds: intrinsically disordered proteins in the norm and pathology, part C. Elsevier Inc.; 2021. p. 1–43. doi: 10.1016/bs.pmbts.2021.06.001
[22] Patel A, Lee HO, Jawerth L, et al. A liquid-to-solid phase transition of the ALS protein FUS accelerated by disease mutation. Cell. 2015;162(5):1066–1077. doi: 10.1016/j.cell.2015.07.047
[23] Elbaum-Garfinkle S. Matter over mind: liquid phase separation and neurodegeneration. J Biol Chem. 2019;294(18):7160–7168. doi: 10.1074/jbc.REV118.001188
[24] Wegmann S, Eftekharzadeh B, Tepper K, et al. Tau protein liquid–liquid phase separation can initiate tau aggregation. Embo J. 2018;37(7):e98049. doi: 10.15252/embj.201798049
[25] Silva JL, Foguel D, Ferreira VF, et al. Targeting biomolecular condensation and protein aggregation against cancer. Chem Rev. 2023;123:9094–9138.
[26] Agarwal A, Rai SK, Avni A, et al. An intrinsically disordered pathological prion variant Y145Stop converts into self-seeding amyloids via liquid–liquid phase separation. Proc Natl Acad Sci USA. 2021;118(45):e2100968118. doi: 10.1073/pnas.2100968118
[27] Matos CO, Passos YM, Amaral MJ, et al. Liquid-liquid phase separation and fibrillation of the prion protein modulated by a high-affinity DNA aptamer. FASEB J. 2020;34(1):365–385. doi: 10.1096/fj.201901897R
[28] Passos YM, Do Amaral MJ, Ferreira NC, et al. The interplay between a GC-rich oligonucleotide and copper ions on prion protein conformational and phase transitions. Int J Biol Macromol. 2021;173:34–43. doi: 10.1016/j.ijbiomac.2021.01.097
[29] Kovachev PS, Gomes MPB, Cordeiro Y, et al. RNA modulates aggregation of the recombinant mammalian prion protein by direct interaction. Sci Rep. 2019;9(1):12406. doi: 10.1038/s41598-019-48883-x
[30] Cordeiro Y, Macedo B, Silva JL, et al. Pathological implications of nucleic acid interactions with proteins associated with neurodegenerative diseases. Biophys Rev. 2014;6(1):97–110. doi: 10.1007/s12551-013-0132-0
[31] Coelho-Cerqueira E, Carmo-Gonçalves P, Sá Pinheiro A, et al. α-synuclein as an intrinsically disordered monomer – fact or artefact? FEBS J. 2013;280(19):4915–4927. doi: 10.1111/febs.12471
[32] Macedo B, Sant'anna R, Navarro S, et al. Mammalian prion protein (PrP) forms conformationally different amyloid intracellular aggregates in bacteria. Microb Cell Fact. 2015;14(1):174. doi: 10.1186/s12934-015-0361-y
[33] Lowry OH, Rosebrough NJ, Farr AL, et al. Protein measurement with the folin phenol reagent. J Biol Chem. 1951;193(1):265–275. doi: 10.1016/S0021-9258(19)52451-6
[34] Paz MM, Ferretti GDS, Martins-Dinis MMC, et al. PRIMA-1 inhibits Y220C p53 amyloid aggregation and synergizes with cisplatin in hepatocellular carcinoma. Front Mol Biosci. 2023;10:10. doi: 10.3389/fmolb.2023.1165132
[35] Andrews S, others. FastQC: a quality control tool for high throughput sequence data. 2010. Available from: http://www.bioinformatics.babraham.ac.uk/projects/fastqc/
[36] Chen S, Zhou Y, Chen Y, et al. Fastp: an ultra-fast all-in-one FASTQ preprocessor. Bioinformatics. 2018;34(17):i884–90. doi: 10.1093/bioinformatics/bty560
[37] Langmead B, Salzberg SL. Fast gapped-read alignment with Bowtie 2. Nat Methods. 2012;9(4):357–359. doi: 10.1038/nmeth.1923
[38] Shen W, Le S, Li Y, et al. SeqKit: a cross-platform and ultrafast toolkit for FASTA/Q file manipulation. PLOS ONE. 2016;11(10):e0163962. doi: 10.1371/journal.pone.0163962
[39] Dobin A, Davis CA, Schlesinger F, et al. STAR: ultrafast universal RNA-seq aligner. Bioinformatics. 2013;29(1):15–21. doi: 10.1093/bioinformatics/bts635
[40] Okonechnikov K, Conesa A, García-Alcalde F. Qualimap 2: advanced multi-sample quality control for high-throughput sequencing data. Bioinformatics. 2016;32(2):292–294. doi: 10.1093/bioinformatics/btv566
[41] Li B, Dewey CN. RSEM: accurate transcript quantification from RNA-Seq data with or without a reference genome. BMC Bioinformatics. 2011;12(1):323. doi: 10.1186/1471-2105-12-323
[42] Liu R, Holik AZ, Su S, et al. Why weight? Modelling sample and observational level variability improves power in RNA-seq analyses. Nucleic Acids Res. 2015;43(15):e97–e97. doi: 10.1093/nar/gkv412
[43] Li H, Handsaker B, Wysoker A, et al. The sequence alignment/map format and SAMtools. Bioinformatics. 2009;25(16):2078–2079. doi: 10.1093/bioinformatics/btp352
[44] Feng J, Liu T, Zhang Y. Using MACS to identify peaks from ChIP-seq data. Curr Protoc Bioinformatics. 2011; 34(1). doi: 10.1002/0471250953.bi0214s34
[45] Feng J, Liu T, Qin B, et al. Identifying ChIP-seq enrichment using MACS. Nat Protoc. 2012;7(9):1728–1740. doi: 10.1038/nprot.2012.101
[46] Wang J, Duncan D, Shi Z, et al. WEB-based GEne SeT AnaLysis Toolkit (WebGestalt): update 2013. Nucleic Acids Res. 2013;41(W1):W77–83. doi: 10.1093/nar/gkt439
[47] Rosenbloom KR, Armstrong J, Barber GP, et al. The UCSC genome browser database: 2014 update. Nucleic Acids Res. 2015;43(D1):D670–81. doi: 10.1093/nar/gku1177
[48] Bailey TL, Williams N, Misleh C, et al. MEME: discovering and analyzing DNA and protein sequence motifs. Nucleic Acids Res. 2006;34:W369–73. doi: 10.1093/nar/gkl198
[49] Bailey TL, Boden M, Buske FA, et al. MEME suite: tools for motif discovery and searching. Nucleic Acids Res. 2009;37(Web Server):W202–8. doi: 10.1093/nar/gkp335
[50] Sato K, Akiyama M, Sakakibara Y. RNA secondary structure prediction using deep learning with thermodynamic integration. Nat Commun. 2021;12(1):941. doi: 10.1038/s41467-021-21194-4
[51] Wang H, Lu X, Zheng H, et al. Rnasmc: a integrated tool for comparing RNA secondary structure and evaluating allosteric effects. Comput Struct Biotechnol J. 2023;21:965–973. doi: 10.1016/j.csbj.2023.01.007
[52] Chan PP, Lowe TM. GtRNAdb 2.0: an expanded database of transfer RNA genes identified in complete and draft genomes. Nucleic Acids Res. 2016;44(D1):D184–9. doi: 10.1093/nar/gkv1309
[53] Maharana S, Wang J, Papadopoulos DK, et al. RNA buffers the phase separation behavior of prion-like RNA binding proteins. Science. 2018;360(6391):918–921. doi: 10.1126/science.aar7366
[54] Do Amaral MJ, Freire MHO, Almeida MS, et al. Phase separation of the mammalian prion protein: physiological and pathological perspectives. J Neurochem. 2023;166(1):58–75. doi: 10.1111/jnc.15586
[55] Kayed R, Head E, Sarsoza F, et al. Fibril specific, conformation dependent antibodies recognize a generic epitope common to amyloid fibrils and fibrillar oligomers that is absent in prefibrillar oligomers. Mol Neurodegener. 2007;2(1):18. doi: 10.1186/1750-1326-2-18
[56] Breydo L, Wu JW, Uversky VN. α-Synuclein misfolding and Parkinson's disease. Biochim Biophys Acta Mol Basis Dis. 2012;1822(2):261–285. doi: 10.1016/j.bbadis.2011.10.002
[57] Zhao S, Zhang Y, Gamini R, et al. Evaluation of two main RNA-seq approaches for gene quantification in clinical RNA sequencing: polyA+ selection versus rRNA depletion. Sci Rep. 2018;8(1):4781. doi: 10.1038/s41598-018-23226-4

[58] Pepke S, Wold B, Mortazavi A. Computation for chip-seq and rna-seq studies. Nat Methods. 2009;6(S11):S22–32. doi: 10.1038/nmeth.1371
[59] Zambelli F, Pavesi G. RIP-seq data analysis to determine RNA-protein associations. Methods Mol Biol. 2015;1269:293–303.
[60] Zhu X, Xie X, Das H, et al. Non-coding 7S RNA inhibits transcription via mitochondrial RNA polymerase dimerization. Cell. 2022;185(13):2309–2323.e24. doi: 10.1016/j.cell.2022.05.006
[61] Blanco A, Blanco G. Chapter 6 – nucleic acids. Elsevier Inc. Medical Biochemistry. 2017:121–140. doi:10.1016/B978-0-12-803550-4.00006-9.
[62] Pang Y, Kurella S, Voisset C, et al. The antiprion compound 6-aminophenanthridine inhibits the protein folding activity of the ribosome by direct competition. J Biol Chem. 2013;288(26):19081–19089. doi: 10.1074/jbc.M113.466748
[63] Tribouillard-Tanvier D, Dos Reis S, Gug F, et al. Protein folding activity of ribosomal RNA is a selective target of two unrelated antiprion drugs. PLOS ONE. 2008;3(5):3. doi: 10.1371/journal.pone.0002174
[64] Silva JL, Vieira TC, Cordeiro Y, et al. Nucleic acid actions on abnormal protein aggregation, phase transitions and phase separation. Curr Opin Struct Biol. 2022;73:102346. doi: 10.1016/j.sbi.2022.102346
[65] Deleault NR, Lucassen RW, Supattapone S. RNA molecules stimulate prion protein conversion. Nature. 2003;425(6959):717–720. doi: 10.1038/nature01979
[66] Cordeiro Y, Freire MHO, Wiecikowski AF, et al. (Dys)functional insights into nucleic acids and RNA-binding proteins modulation of the prion protein and α-synuclein phase separation. Biophys Rev. 2023;15(4):577–589. doi: 10.1007/s12551-023-01067-4
[67] Beaudoin S, Vanderperre B, Grenier C, et al. A large ribonucleoprotein particle induced by cytoplasmic PrP shares striking similarities with the chromatoid body, an RNA granule predicted to function in posttranscriptional gene regulation. Biochim Biophys Acta Mol Cell Res. 2009;1793(2):335–345. doi: 10.1016/j.bbamcr.2008.10.009
[68] Wolozin B, Ivanov P. Stress granules and neurodegeneration. Nat Rev Neurosci. 2019;20(11):649–666. doi: 10.1038/s41583-019-0222-5
[69] Roucou X. Prion protein and RNA: a view from the cytoplasm. Front Biosci. 2009;14(1):5157–5164. doi: 10.2741/3592
[70] Muñoz-Gutiérrez JF, Pierlé SA, Schneider DA, et al. Transcriptomic determinants of scrapie prion propagation in cultured ovine microglia. PLOS ONE. 2016;11(1):e0147727. doi: 10.1371/journal.pone.0147727
[71] Brown CA, Schmidt C, Poulter M, et al. In vitro screen of prion disease susceptibility genes using the scrapie cell assay. Hum Mol Genet. 2014;23(19):5102–5108. doi: 10.1093/hmg/ddu233
[72] Saá P, Sferrazza GF, Ottenberg G, et al. Strain-specific role of RNAs in prion replication. J Virol. 2012;86(19):10494–10504. doi: 10.1128/JVI.01286-12
[73] Sayer NM, Cubin M, Rhie A, et al. Structural determinants of conformationally selective, prion-binding aptamers. J Biol Chem. 2004;279(13):13102–13109. doi: 10.1074/jbc.M310928200
[74] Petronilho EC, Pedrote MM, Marques MA, et al. Phase separation of p53 precedes aggregation and is affected by oncogenic mutations and ligands. Chem Sci. 2021;12(21):7334–7349. doi: 10.1039/D1SC01739J